Experimental charge density of LiBD_{4} from maximum entropy method

F. Buchter, Z. Lodziana, A. Remhof, Ph. Mauron, O. Friedrichs, A. Borgschulte, A. Züttel, Y. Filinchuk, and L. Palatinus

Phys. Rev. B **83**, 064107 — Published 22 February 2011

DOI: 10.1103/PhysRevB.83.064107

BV11518

Experimental charge density of $LiBD_4$ from maximum entropy method

F. Buchter,[*] Z. Łodziana, A. Remhof, Ph. Mauron, O. Friedrichs, A. Borgschulte, and A. Züttel[†]
Empa, Swiss Federal Laboratories for Materials Testing and Research, Laboratory for Hydrogen & Energy
Überlandstrasse 129, CH-8600 Dübendorf, Switzerland

Y. Filinchuk
European Synchrotron Radiation Facility,
Swiss-Norwegian Beamlines
BP 220, F-38043 Grenoble, France

L. Palatinus
Laboratoire de Cristallographie, Le Cubotron, Ecole Polytechnique Fdrale de Lausanne, 1015 Lausanne, Switzerland

(Dated: January 4, 2011)

We report on maximum entropy method study of the experimental atomic and ionic charges of $LiBD_4$ in its low temperature orthorhombic phase. Synchrotron radiation X-ray powder diffraction data, neutron powder diffraction data,and density functional calculations were used. The atomic and ionic charges were determined for both experimental and theoretical results using the Bader analysis for atoms in molecules. The charge transfer from the Li cation the the BH_4 anion is of 0.86(±9) e, which is in good agreement with the ab-initio calculated value of 0.895 e. The experimental accuracy was determined considering the differences between results obtained for data collected at 10 K and 90 K, different experimental setup (high resolution diffractometer or image plate diffractometer), and different structural models used for the prior density distributions needed for accurate maximum entropy calculations (refined against only synchrotron radiation X-ray powder diffraction data, or combined with neutron powder diffraction data).

PACS numbers:

I. INTRODUCTION

Among different techniques to store hydrogen,[1,5] solid state hydrogen storage in alkali, alkaline earth, and transition metal tetrahydroborates $M(BH_4)_n$ (M = Li, Na, K, Mg, Ca, Sc, Ti, Zn, Zr, Al, etc.; n = 1,2,3,4) is focusing a lot of interest owing to the high hydrogen content of these compounds.[3–6] Some of the most promising tetrahydroborates ($Li(BH_4)$, $Ca(BH_4)_2$, $Mg(BH_4)_2$) exhibit high decomposition temperatures related to either thermodynamic or kinetic reasons.[3–6] Beside kinetics, the key issue to control the temperature of hydrogen release in tetrahydroborates (i.e. their stability) is to act on the strength of the B-H covalent bond. Understanding the parameters/phenomena driving the B-H bond strength allows control of the stability of tetrahydroborates.

The role played by the anionic charge in the BH_4 stability has recently been pointed out by several authors.[2,7–10] Complementary to works directly considering the role of the anionic electronic density,[9,10] further support was brought by works considering either the decomposition temperature T_{dec} or formation enthalpy ΔH_0 of selected tetrahydroborates with respect to the Pauling electronegativity χ of the constituting cations M.[2,7,8] An illustration of some practical ability of such a relationship to suggest a choice of cation or combination of mixed cations matching an expected T_{dec} was provided recently for the first mixed alkali tetrahydroborates[11] (disregarding segregation issues, and assuming an average Pauling electronegativity of the two individual cations). However, so far no experimental ionic charges of tetrahydroborates are available in the literature to the knowledge of the authors.

X-ray diffraction data carries the information about the electronic charge density in the observed structure factors $F_{obs}(\mathbf{H})$ extracted from the measured reflections intensities. Thereby $\mathbf{H} = h\mathbf{a} + k\mathbf{b} + l\mathbf{c}$ is the lattice vector of the reflection, $\mathbf{a}, \mathbf{b}$ and $\mathbf{c}$ are the basic vectors of the reciprocal lattice and h, k and l are the Miller indicees. In principle, the electronic charge density in the unit cell is the direct Fourier transform of an infinity of $F_{obs}(\mathbf{H})$. Practically, the wavelength used in the experiment limits the information available by fixing the number of measured $F_{obs}(\mathbf{H})$, hence the Fourier transform is affected by series terminations errors (e.g. unphysical local minima of the density with negative charge may occur). In addition growing a single crystal of alkali tetrahydroborate is very difficult, and powder samples were used in the present work. Compared to single crystal diffraction, the powder averaging of the diffraction data further reduces the information contained in it. These two limitations in the available information ($\sin\theta/\lambda \approx 0.6$ Å^{-1}, and powder diffraction data) prevent a reasonable use of multipole refinement of the density distribution in the unit cell. Therefore, the maximum entropy method[12–16] (MEM) was used to maximize the information extracted from the intrinsically limited experimental data, and determine the corresponding electronic charge distribution in the lattice, while ensuring the positivity of the distribution. It has been already demonstrated that synchrotron radiation X-ray powder diffraction (SR-XPD) data may be used to determine electronic charge density distributions using MEM.[16–20] Such distributions are of enough quality to discuss disorder, thermal displacements, and as in the present work, integrated atomic charges.[16–20] As part of Bayesian statistics, the MEM makes use of prior information on the system. It is provided in the present case by the electronic distribution corresponding to a refined independent-atom model (IAM) using the same experimental data.[16,20,21] In the MEM, the unit cell is divided in grid of $N_p = N_a \times N_b \times N_c$ pixels. The entropy of the system is defined as

$$S = -\sum_{i=1}^{N_p} \rho_i \log\left(\rho_i/\tau_i\right)$$

considering the density ρ_i of each pixel, and its prior density τ_i. τ_i introduces in the entropy the prior information that we have about the system before the MEM calculation. The ρ_i are adjusted so that S is maximized under the constraint

$$\chi^2 = \sum_{hkl} \frac{\left|F_{obs}(\mathbf{H}) - F_{MEM}(\mathbf{H})\right|^2}{\sigma_{obs}(\mathbf{H})^2} = C$$

where $F_{MEM}(\mathbf{H})$ are the structure factors corresponding to the final calculated distribution ρ, and C is the total number of individual reflections. Higher moments than 2^{nd} moment χ^2 might be used under certain circumstances.[26] It is worth to keep in mind that the experimental data is introduced in the MEM via the $F_{obs}(\mathbf{H})$ and $\sigma_{obs}(\mathbf{H})$, but also via the prior distribution τ obtained by refinement of a IAM model. Therefore, unless additional information is introduced in this model (e.g. considering neutron diffraction data complementary to X-ray data for the refinement of the structural model), MEM consist simply in a more subtle and complete use of the experimental diffraction data which is in principle model-free if the experimental data is of sufficient quality (i.e. $F_{obs}(\mathbf{H})$ and $\sigma_{obs}(\mathbf{H})$ independent on the IAM model).

In addition to methodological precautions required for an approriate use of MEM[16,20–27] (use of prior density distribution, order and distribution of normalized residuals, prior-derived F constraints), particularities related to the investigated system constituted of light atoms and the used experimental instrumental setup imposed additional considerations. This is particularly important for the choice of an appropriate refined IAM used for the treatment of the overlapped diffraction peaks, and providing the prior density distribution for the MEM calculations. The difficulty here is the somewhat inadequateness of the IAM for hydrogen atoms consisting of a single valence electron (no core electron) involved in a covalent bond with boron.

In the present work, we report on the experimental determination of the electronic charge density of $LiBD_4$ in its low temperature orthorhombic phase using SR-XPD data and MEM (four phases are reported[28] to date for $LiBH_4$). Two different instrumental setups have been considered for their specific characteristic: 1) A high-resolution powder diffractometer for reducing peak overlap; 2) An image plate area detector diffractometer for the accuracy of the measured intensities and the high signal to noise ratio. Integrated ionic charges of the Li cation and BD_4 anion, as well as the charges of individual atoms have been determined applying Bader analysis[29] to the experimental electronic charge distribution. The accuracy of the experimental charges has been evaluated comparing integrated atomic charges obtained for the different measurement temperatures, instrumental setups, and combination of data (used to refine the structural model providing the prior distribution and used for the extraction of $F_{obs}(\mathbf{H})$ from the data). Experimental results are discussed on the same basis and compared to density functional theory (DFT) calculated electronic density distribution.

II. EXPERIMENTAL

The powder of $LiBD_4$ (purity $> 95\%$) was purchased from Katchem Ltd. and the samples were always handled in vacuum, argon or helium atmosphere. All the measurements were performed using the same sample batch, except for neutron powder diffraction (NPD) data at 10 K obtained from a previous work on $LiBD_4$.[30] SR-XPD data was collected at 90 K using a MAR345 image plate detector at the Swiss-Norwegian beamlines (SNBL-BM01A) at the European Synchrotron Radiation Facility (ESRF) in Grenoble (France). The sample was filled into 0.7 mm diameter glass capillaries, the wavelength was 0.711710 Å, and the temperature was controlled by an Oxford Cryostream 700+ blower (90 K was the lower accessible temperature for this setup). Data was collected at three different detector-sample distances (150 mm, 200mm, 300mm). SR-XPD data was collected at 10 K and 90 K on the high-resolution powder diffractometer of the material science (MS) beamline at the Swiss Light Source (SLS) at the Paul Scherrer Institute (PSI) in Villigen (Switzerland). The samples were filled into 1.0 mm diameter glass capillaries, the wavelength was 0.954795 Å, and the temperature was controlled by a Janis He-flow cryostat with integrated spinner.

NPD data was collected at 90 K at the high resolution powder diffractometer for thermal neutrons (HRPT) at the Swiss spallation neutron source (SINQ) at the PSI. The sample was filled into a double-walled vanadium cylinder of 9 mm outer diameter, 7 mm inner diameter, and 50 mm length, the wavelength was 1.494 Å, and the temperature was controlled by means of a closed-cycle He refrigerator mounted in an evacuated aluminum vessel. The absorption correction coefficient $\mu R = 0.225$ was determined by transmission measurements.

The structural model of the orthorhombic low temperature phase[30–34] of $LiBD_4$ was refined using the program FULLPROF[35] (version 3.80) against either SR-XPD data or combined SR-XPD/NPD data (see details of the refinement in supporting information). The phased observed structure factors $F_{obs}(\mathbf{H})$ resulting from the refinement (with corresponding standard deviation) were corrected for anomalous dispersion[17] and used for the MEM calculations. When SR-XPD data from the image plate detector is used, $F_{obs}(\mathbf{H})$ corresponding to low scattering angles are extracted from the largest detector-sample distance data (300 mm), respectively $F_{obs}(\mathbf{H})$ corresponding to intermediate/high scattering angles are extracted from the middle/shortest detector-sample distance data (200 mm/150mm). Doing so optimizes the data collection by improving the resolution of the low $\sin\theta/\lambda$ reflections (these are the reflections mostly affected by charge distributions far from the nucleus, i.e. involved in covalent bonds), while still covering a sufficient $\sin\theta/\lambda$ range. To reduce well known artifacts of MEM resulting from series termination errors,[23,27] the refined models were used to generate a density distribution corresponding to a procrystal,[36] which was used as prior distribution for MEM calculations. The MEM calculations were performed using the software BayMEM.[37] A 144 x 88 x 140 pixel grid along the crystallographic axis a, b and c was used for MEM calculations, corresponding to ~ 0.05 Å of pixel resolution in each direction (i.e. the shortest interatomic distances correspond to ~ 25 pixels). The resulting density distributions are presented in Fig. 1, Fig. 2, and Fig. 3.

In the supporting information we discuss the influence on the final MEM density distribution of: The intrinsic influence of the refined structural model on the sharing of the total intensity of a group of overlapping reflections among individual reflections, using G-constraints[39] (i.e. with and without considering strongly overlapping reflections[38] as single group-structure factors $G_{obs}(\mathbf{H})$ called G-groups); The prior density distribution considering different structural models for a given set of $F_{obs}(\mathbf{H})$; The order of the statistical central moment of the normal residuals of the structure factors;[26] The use of additional prior information from the refined structural models for higher scattering angles $\sin\theta/\lambda \geq 0.6$ Å^{-1}, via prior-derived F constraints.[27]

MEM distribution at 10 K (i.e. at the lowest temperature where thermal smearing of the true electronic charge is minimized) is compared to DFT calculated electronic density distributions. Detail about DFT calculation of $LiBD_4$ are extensively described elsewhere.[30] The DFT calculated structures were either optimized with constrained symmetry, until the forces exerted on atoms were smaller than 0.01 eV/Å (corresponding shape and volume of the unit cell was relaxed and the procedure was repeated until self-consistency was achieved), or the unit cell size and nucleus were kept fixed at the experimental values of the refined structural model.

Atomic charges were subsequently determined applying the Bader analysis for atoms in molecules to the MEM and DFT distribution,[29] using the program EDMA[37] (see Table I, Table II, and Table III). Atomic basins in the MEM or DFT distributions are determined by this method considering a division of the distribution into subsystems separated by zero density flux surfaces. Critical points[29] of the density distribution (i.e. points where the density gradient vanishes) corresponding to local maximum of the density are attributed to the basin into which they are found, and linked to the closest atom of the structural model lying in this basin. Finally, the integrated charge within a basin is fully attributed to the corresponding atom.

III. RESULTS AND DISCUSSION

In the first part of this section, technical aspects of the MEM calculations of the electronic density distribution of light complex hydrides are discussed. In the second part, the electronic density distribution and integrated atomic/ionic charges of $LiBD_4$ are discussed.

A. MEM calculations

The main factor influencing the final MEM distributions is the choice of an appropriate structural model to generate the prior distribution used in the MEM calculations (see Fig. 1, Fig. 2, Fig. 3, Table I). To some extent, this reflects the degree of inaccuracy in the data (see supporting information).

In order to understand the major differences between the prior density distributions resulting from structural refinements against SR-XPD data or combined SR-XPD/NPD data, one has to consider the covalent bond involving the light atoms B and D in the BD_4 tetrahedra. In the B-D covalent bond, part of the electronic charge of the B and D atoms is shared. This implies a difference between the center of mass of the atomic nucleus (CMN), which is close to the real atomic center of mass, and the center of mass of the atomic electronic distributions (CMED). In the present case, refining the $LiBD_4$ structural model against SR-XPD data result in atomic positions close to the CMED. For the heavier atoms with core electrons (Li and B), the CMED is in fact close to the CMN, while this is not the case for D atoms (see supporting information). Refining the $LiBD_4$ structure against combined SR-XPD and NPD data takes advantage of both radiations to accurately locate the heavier atoms B and Li thanks to their high X-ray scattering power (as explained before, their CMED is close to their CMN), and accurately locate the D atoms close to the CMN thanks to the high D neutron scattering power. The same holds for atomic displacement parameters (ADP): If SR-XPD/NPD data is used, the contribution of atomic displacements to ADP reflects mostly nucleus displacements, i.e. of the CMN; If SR-XPD is used, the contribution of atomic displacements to ADP reflects displacements of the CMED. Additionally, ADP reflects not only averaged atomic displacements, but also partly the deviation of the true scattering distribution from the IAM distribution (e.g. due to covalent bonds). The relative influence of these two contributions on the ADP may differ, depending on the data used for the refinement of the structural model, and the type of atom. Therefore, unless the CMN and CMED are close ones from each others (e.g. atoms with a large valence/core electrons ratio), significant differences between atomic coordinates and ADP obtained from the refinement of a IAM against SR-XPD or SR-XPD/NPD data may be expected for light atoms involved in covalent bonds.

Based on the previous discussion, it is very difficult to determine -a priori- the most appropriate prior distribution. As discussed above, an IAM refined against SR-XPD/NPD data is the most appropriate choice for an accurate determination of the atomic structure (atomic positions and ADP corresponding closely to the ones of the real center of mass of the atoms). In an IAM refined against SR-XPD the interpretation of the ADP is not so straight forward (due to the deviation of the true scattering distribution from the IAM distribution discussed above), however it provides atomic positions close to the CMED. It is hence likely that this prior distribution with individual atomic distributions centered on the CMED, and ADP taking into account the combined effect of the thermal displacements and the deviation from the IAM distribution is better suited for a electronic distribution study. However, in order to fully verify this assertion, any reference system/data for light complex hydrides is so far missing. Therefore the differences observed between MEM distributions obtained based on the different prior distributions prevent any detailed discussion of fine bond features, especially for low density regions like D atoms. Nevertheless, the MEM distributions are of sufficient quality to reliably extract integrated atomic charges from it, as will be discussed below for the $LiBD_4$ case study. The difference in the integrated atomic charges resulting from the use of different priors was in fact used to determine the accuracy in a very conservative way.

The treatment of overlapping diffraction peaks using G-constraints was sufficient to reduce the influence of the refined structural model used to extract the set of $F_{obs}(\mathbf{H})$ to a level such that similar fine features of the electronic charge distributions are exhibited by MEM charge densities obtained for sets of $F_{obs}(\mathbf{H})$ resulting from refined structural models against SR-XPD or combined SR-XPD/NPD data (see supporting information). The MEM distributions obtained based on these two possible refined IAM, with and without use of G-constraint, are illustrated in Fig. 1. No significant effect has been observed using high-order central moments for the distribution of the residuals of the structure factors (see Table II, Table III, and supporting information). Due to the limited range of measured scattering angles ($\sin\theta/\lambda \approx 0.6$ Å^{-1}), the prior-derived F constraints could not be considered (see Table II, Table III, and supporting information).

In our attempt to compare results obtained for two different setups for the measurement of SR-XPD data (high resolution diffractometer and image plate detector diffractometer), we found an excellent agreement between the final MEM distributions with G-constraints corresponding to the two setups (see Fig. 2, Fig. 3, and Table III). This simultaneously validates the collection of data using an image plate detector, and the treatment of overlapped reflections by G-constraints. As long as a good powder averaging is achieved in the sample, it is better to use data collected on a high resolution diffractometer. The reason is the larger ratio of the number of independent reflections versus the number of reflections included in a G-group for high resolution data (≈60% in the present case, see Table III), compared to image plate detector data (≈30% in the present case, see Table III -note that the wavelength is different compared to high resolution data-). A larger number of independent reflections ensures a better independence of the $F_{obs}(\mathbf{H})$ with respect to the chosen IAM model. Actually, for independent reflections, the IAM model only influences the $F_{obs}(\mathbf{H})$ through the scale factor needed to account for the data collection statistics. The lower resolution of an image plate detector increases the dependence of the MEM density distributions on the refined structural used for the sharing of the total intensity of a group of overlapped reflections among individual reflections (see supporting information). However, the total intensity of a G-group is in fact as independent on the IAM model as an individual independent reflection (see supporting information). Therefore for sample with poor powder averaging, data collection of sufficient quality can be obtained by means of an image plate diffractometer (the whole Bragg rings are integrated, thus averaging the intensity as would do a good powder averaging).

B. Density distribution of $LiBD_4$

It is a general trend for all measurements (considering all temperatures and setups) that with respect to the prior distributions, part of the electronic charge of the B atom in the IAM procrystal is redistributed over the D atoms in the MEM density distribution (see Fig. 2, Fig. 3, and Table III). This trend emphasizes the additional information extracted from the data, and not contained in the IAM prior.

Comparing MEM distributions with G-constraints, it appears that the charges determined by Bader analysis for the Li atom and the BD_4 group are less affected by the choice of the prior than the charges of the B and D atoms (see Table I compared to Table II and Table III). To understand this effect, one should keep in mind the weak density of D, and the covalent nature of the B-D bond. In a simplified picture, any change in the prior distribution will affect the final density distribution, particularly the curvature of the density close to the border of the atomic basins (hence the shape of the zero-density flux surfaces determined by the Bader analysis). The effect on the size of two neighboring basins (consequently on the integrated charge of the basins) may differ depending on the maximum charge of the basins and the charge at the border (zero-flux surface) between the two basins. E.g. the ratio between the minimum of the density along the B-D bond and the maximum density of D is much larger than the ratio between the minimum of the density along the Li-B bond and the maximum density of Li (see in Fig. 4). A change in the MEM distribution likely affects more the critical points defining basins of atoms with a large ratio (e.g. between B and D) than the critical points defining basins of atoms with a little ratio (e.g. between Li and B, or Li and D) as illustrated in Fig. 4. One should however also keep in mind that a reasonably good prior density is still required, since a uniform prior density may give quite different misleading results (see Table II and Table III).

As an second general trend, MEM distributions based on a structural model refined against SR-XPD data systematically concentrate more charge on the D atoms than MEM distributions based on a structural model refined against combined SR-XPD/NPD data (see Fig. 5). As discussed above and in supporting information, this effect is a direct consequence of the influence of the prior density on the final MEM distribution (see supporting information), and is due to the differences between the prior distributions that exhibit actually the same trend.

As expected, the difference between MEM distributions obtained at 10 K and at 90 K emphasizes the smearing effect of increased thermal motion of the atoms at 90 K on the resulting MEM distributions (see Fig. 2 and Fig. 3 compared to Fig. 1). Although this effect has a minor influence on the atomic charge obtained applying the Bader analysis (see Table II and Table III).

Summarizing the several technical aspects discussed in this section, we conclude that for light tetrahydroborates (or more generally light hydrogen-based systems), the best MEM distribution based on SR-XPD data is obtained from: The use of high resolution powder diffraction data, as long as a good powder averaging is not an issue; A data collected at the lowest possible temperature (in the present case 10 K); The use of a prior distribution obtained from an IAM refined against SR-XPD data; The use of G-constraint for strongly overlapping reflections.

Accordingly, the atomic charges of the line 1.2 in Table II were considered as best experimental atomic charges. The experimental accuracy was determined by the difference between the extreme values of atomic charge (for each single atom) considering MEM distributions obtained at 10 K and 90 K (the two setups are considered) with the different prior distributions (i.e. considering the cases: 1.2 and 1.6 in Table II; 2.2 and 2.5, 2.10 and 2.18 on Table III). Since this estimate of the interval of accuracy does not correspond to the standard uncertainty (one sigma of a normal distribution), an additional "±" was used inside the usual bracket notation of uncertainty to notify it. The experimental atomic/ionic charges are: Li = 2.14(±9) e, B = 3.91(±35) e, D1 = 1.50(±14) e, D2 = 1.56(±18) e, D3 = 1.45(±10) e, DH_4 = 9.86(±9) e.

As mentioned earlier, no detailed discussion of the experimental electronic distribution was attempted. However, a couple of general observations may be discussed within the experimental accuracy. First of all, it has to be emphasized that the usual ionic picture of $LiBD_4$ (Li^+ cations and BD_4^- anions) with D covalently bonded to B holds. This is not only borne out in the experimental charge transfer of 0.86±9 e from Li atoms to BD_4 groups, but is also qualitatively visible in Figure 4. Indeed, in Figure 4 the charge density along the Li-B bond exhibit a minimum close to ~ 0 e/Å^3, while the minimum of density along the B-D bond is much larger (i.e. roughly half of the maximum density of D). This last observation holds, even comparing the different density distributions obtained for to the two considered priors. The difference between the two distributions at their minima along the B-D bond is indicated by arrows in Figure 4, and is in fact much smaller than the total density at the same position. Finally, comparing experimental MEM density distributions to DFT calculations, as displayed in Figure 6, it appears that the best agreement is obtained with the MEM density distribution obtained indeed at 10 K with a prior density distribution from a IAM model refined against SR-XPD data (see Figure 6 and Table II). This further reinforces our deduction of the best experimental distribution among the many calculated in this work.

IV. CONCLUSION

The atomic and ionic charges density of $LiBD_4$ have been experimentally determined using synchrotron radiation X-ray powder diffraction data and the maximum entropy method (MEM). The best MEM distribution was obtained from high resolution synchrotron radiation X-ray powder diffraction (SR-XPD) data collected at 10 K, and MEM calculations using G-constraint for strongly overlapping reflections and a prior distribution obtained from an IAM refined against SR-XPD data. The experimental atomic and ionic charges are: Li = 2.14(±9) e, B = 3.91(±35) e, D1 = 1.50(±14) e, D2 = 1.56(±18) e, D3 = 1.45(±10) e, BD_4 = 9.86(±9) e. The corresponding charge transfer from the Li cation the the BD_4 anion is of 0.86(±9) e, in good agreement with the value of 0.895 e calculated by the density functional theory and the usual ionic picture of $LiBH_4$. The role of the prior density distribution for the calculation of the MEM density distributions has been carefully investigated and provided a way to determine the experimental accuracy of the atomic and ionic charges. An excellent consistency has been observed between experimental results obtained for data collected at 10 K and 90 K, considering different experimental setup (high resolution diffractometer or image plate diffractometer), and different structural models used for the prior density distributions (refined using only SR-XPD data, or SR-XPD data combined with neutron powder diffraction data). This reinforces the validity of the approach considered in this work to determine experimental density distributions, which may be extended to many other light hydrogen-based systems. It also demonstrates the possibility to collect SR-XPD data with an image plate detector diffractometer, opening a window on possible fast measurements (order of magnitude of few minutes) allowing to scan many temperature conditions.

Acknowledgments

We highly appreciated skillful assistance from F. Gozzo at the MS beamline at the SLS (PSI, Villigen, Switzerland), and D. Sheptyakov at HRPT instrument at the SinQ (PSI, Villigen, Switzerland). CPU time allocation at CSCS supercomputer center (Manno) is kindly acknowledged. Financial support by the Swiss National Science Foundation (Schweizerischer Nationalfonds, SNF), project No. 200020-115875 is gratefully acknowledged.

---

[*] Also at University of Fribourg, Physics Department, CH-1700 Fribourg, Switzerland; Electronic address: `florian.buchter@empa.ch`

[†] Also at University of Fribourg, Physics Department, CH-1700 Fribourg, Switzerland

[1] L. Schlapbach and A. Züttel, Nature **414(15)**, 353-358 (2001).

[2] W. Grochala, P. Edwards, Chem. Rev. *104*, 1283 (2004).

[3] A. Züttel, A. Borgschulte, and S. Orimo, Scr. Mater. **56**, 823-828 (2007).

[4] S. Orimo, Y. Nakamori, J. Eliseo, A. Züttel, and C. M. Jensen, Chem. Rev. **107**, 4111-4132 (2007).

[5] A. Züttel, A. Borgschulte, and L. Schlapbach, Hydrogen as a Futre Energy Carrier, Wiley (2008).

[6] Y. Filinchuk, D. Chernyshov, V. Dmitriev, Z. Kristallogr. **223**, 649-659 (2008).

[7] Y. Nakamori, H. W. Li, K. Miwa, S. Towata, S. Orimo, Mater. Trans. **47**, 1898-1901 (2006).

[8] Y. Nakamori, K. Miwa, A. Ninomiya, H. Li, N. Ohba, S. Towata, A. Züttel, S. Orimo, Phys. Rev. B **74**, 045126 (2006).

[9] A. J. Du, S. C. Smith, and G. Q. Lu, Phys. Rev. B **74**, 193405 (2006).

[10] Z. Łodziana, A. Züttel, P. Zielinski, J. Phys.: Condens. Matter **20**, 465210 (2008).

[11] E. A. Nickels, M. O. Jones, W. I. F. David, S. R. Johnson, R. L. Lowton, M. Sommariva, P. Edwards, Angew. Chem. Int. Ed., **2008**, 47, 2817-2819.

[12] E.T. Jaynes, Physical Review **106**, 620-630 (1957).

[13] S. F. Gull, G. J. Daniel, Nature **272**, 686-690 (1978).

[14] D. M. Collins, Nature **298**, 49-51 (1982).

[15] M. Sakata, M. Sato, Acta Crystallogr. A **46**, 263-270 (1990).

[16] C. J. Gilmore, Acta Crystallogr. A **52**, 561-589 (1996).

[17] B. Bagautdinov, J. Luedecke, M. Schneider, S. van Smaalen, Acta Crystallogr. B **54**, 626-634 (1998).

[18] R. E. Dinnebier, M. Schneider, S. Van Smaalen, F. Olbrich, U. Behrens, Acta Crystallogr. B **55**, 35-44 (1999).

[19] T. Noritake, M. Aoki, S. Towata, Y. Seno, Y. Hirose, E. Nishibori, M. Takata, M. Sakata, Applied Physics Letters **81**, 2008-2010 (2002).

[20] M. Merli, A. Pavese, Z. Kristallogr. **221**, 613-620 (2006).

[21] P. Roversi, J. J. Irwin, G. Bricogne, Acta Crystallogr. A **54**, 971-996 (1998).

[22] W. Jauch, A. Palmer, Acta Crystallogr. A **49**, 590-591 (1993).

[23] W. Jauch, Acta Crystallogr. A **50**, 650-652 (1994).

[24] B. B. Iversen, F. K. Larsen, M. Souhassou, M. Takata, Acta Crystallogr. B **51**, 580-591 (1995).

[25] De Vries, R. Y., Briels, W. J., Feil, D., Physical Review Letter **77**, 1719-1722 (1996).

[26] L. Palatinus, S. van Smaalen, Acta Crystallogr. A **58**, 559-567 (2002).

[27] L. Palatinus, S. van Smaalen, Acta Crystallogr. A **61**, 363-372 (2005).

[28] V. Dmitriev, Y. Filinchuk , D. Chernyshov, A. V. Talyzin, A. Dzwilewski, O. Andersson, B. Sundqvist, A. Kurnosov, Phys. Rev. B **77**, 174112 (2008).

[29] R. F. W. Bader, Atoms in Molecules: A Quantum Theory, Clarendon Press, Oxford Science Publications (1990).

[30] F. Buchter, Z. Łodziana, Ph. Mauron, A. Remhof, O. Friedrichs, A. Borgschulte, A. Züttel, D. Sheptyakov, T. Strässle, A. J. Ramirez-Cuesta, Phys. Rev. B, *78*, 094302 (2008).

[31] J-Ph. Soulié, G. Renaudin, R. Černý, K. Yvon, J. Alloys Compd. **346**, 200-205 (2002).

[32] A. Züttel, S. Rentsch, P. Fisher, P. Wenger, P. Sudan, Ph. Mauron, Ch. Emmenegger, J. Alloys Compd. **356-357**, 515-520 (2003).

[33] M. Hartman, J. Rush, T. Udovic, R. Bowman Jr., Son-Jong Hwang, J. Solid State Chem. **180** 12981305 (2007).

[34] Y. Filinchuk, D. Chernyshov, R. Černý, J. Phys. Chem. C., In press.

[35] J. Rodríguez-Carvajal, Physica B **192**, 55 (1993).

[36] Eletron densities of neutral atom from IAM model convoluted with occupation probability distribution corresponding to the refined atomic thermal displacements.

[37] S. van Smaalen, L. Palatinus, M. Schneider, Acta Crystallogr. A **59**, 459-469 (2003).

[38] Overlapping reflections not resolved for intensities above half of the reflection maxima.

[39] M. Sakata, R. Mori, S. Kumazawa, M. Takata, H. Toraya, J. Appl. Cryst **23**, 526-534 (1990).

See EPAPS Document No. [] for detailed information on (A) the Rietveld refinements, (B) the influence of the refined structural model on the sharing of the total intensity for overlapping reflections, with and without G-constraints, (C) the influence of prior density distribution considering different structural models for a given set of $F_{obs}(H)$, (D) the influence of the order of the statistical central moment of the normal residuals of the structure factors and (E) the Influence of the use of prior-derived F constraints.

Figures

FIG. 1: MEM density distribution for SR-XPD data 10 K. The diffraction pattern was recorded using the high-resolution powder diffractometer of the material science (MS) beamline at the Swiss Light Source (SLS). Left: $F_{obs}(\mathbf{H})$ from combined SR-XPD/NPD refined model; Right: $F_{obs}(\mathbf{H})$ from SR-XPD refined model. Top: prior density distribution; Middle: MEM density distribution; Bottom: MEM density distribution with G-constraints. Contour intervals 0.2 e /Å^3, cutoff level 5 e /Å^3. Plane cutting D1, D2, and B atoms; Li: green; B: blue; D: red.

FIG. 2: MEM density distribution for SR-XPD data at 90 K. The diffraction pattern was recorded using the high-resolution powder diffractometer of the material science (MS) beamline at the Swiss Light Source (SLS). Left: $F_{obs}(\mathbf{H})$ from combined SR-XPD/NPD refined model; Right: $F_{obs}(\mathbf{H})$ from SR-XPD refined model. Top (A): prior density distribution; Middle (B): MEM density distribution with G-constraint; Bottom: Difference final-prior (B-A). Contour intervals 0.2 e /Å^3, cutoff level 5 e /Å^3. Contour intervals for difference plot 0.02 e /Å^3. Plane cutting D1, D2, and B atoms; Li: green; B: blue; D: red.

FIG. 3: MEM density distribution for SR-XPD data at 90 K. The diffraction pattern was recorded using a MAR345 image plate detector at the Swiss-Norwegian beamline (SNBL-BM01A at the European Synchrotron Radiation Facility (ESRF). Left: $F_{obs}(\mathbf{H})$ from combined SR-XPD/NPD refined model; Right: $F_{obs}(\mathbf{H})$ from SR-XPD refined model. Top (A): prior density distribution; Middle (B): MEM density distribution with G-constraint; Bottom: Difference final-prior (B-A). Contour intervals 0.2 e /Å^3, cutoff level 5 e /Å^3. Contour intervals for difference plot 0.02 e /Å^3. Plane cutting D1, D2, and B atoms; Li: green; B: blue; D: red.

FIG. 4: Electronic density along the Li-B, and B-D directions indicated by the two dashed lines in inset (ii). Solid line: MEM density distribution for data at 10 K with G constraints (prior distribution and $F_{obs}(\mathbf{H})$ from SR-XPD refined model); Dashed line: MEM density distribution for data at 10 K with G constraints (prior distribution and $F_{obs}(\mathbf{H})$ from combined SR-XPD/NPD refined model). Inset (i): Magnification along part of the Li-B, and B-D directions. Minimum of density along the lines are marked by arrows labeled (a) and (b), qualitatively indicating the atomic basin separations: (a) from SR-XPD refined model; (b) from combined SR-XPD/NPD refined model. Inset(ii): Plane cutting D1, D2, and B atoms. Contour intervals 0.2 e /Å^3, cutoff level 5 e /Å^3.

FIG. 5: Difference (final-prior) MEM density distribution for data at 10 K with G constraints. Left: $F_{obs}(\mathbf{H})$ from combined SR-XPD/NPD refined model; Right: $F_{obs}(\mathbf{H})$ from combined SR-XPD refined model. Contour intervals 0.02 e /Å^3. Plane cutting D1, D2, and B atoms; Li: green; B: blue; D: red.

FIG. 6: DFT density distributions: Top left (A): lattice and atomic coordinates from model refined with SR-XPD data at 10 K; Top right (B): lattice and atomic coordinates relaxed; Bottom left (C): MEM density distribution for data at 10 K with G constraints ($F_{obs}(\mathbf{H})$ from combined SR-XPD refined model); Bottom right (D): Difference (C-A) between MEM distribution (C) and DFT distribution (A). Contour intervals 0.2 e /Å^3, cutoff level 5 e /Å^3. Contour intervals for difference plot 0.1 e /Å^3. Plane cutting D1, D2, and B atoms; Li: green; B: blue; D: red.

Tables

TABLE I: Prior and DFT density distributions, and corresponding atomic integrated charges.

Case	Description	T (K)	Li (e)	B (e)	D1/D2/D3 (e)	BD_4 (e)
I	X-HR	10	2.17586	4.45427	1.38375/1.32234/1.33113	9.82262
II	XN-HR	10	2.21906	4.75303	1.30423/1.25548/1.23425	9.78124
III	X-HR	90	2.18810	4.44238	1.39047/1.33446/1.32265	9.81261
IV	XN-HR	90	2.23951	4.78615	1.30485/1.23030/1.21920	9.7597
V	X-IP	90	2.22578	4.51273	1.36064/1.28383/1.30606	9.76932
VI	XN-IP	90	2.25298	4.79397	1.31668/1.19753/1.21921	9.7466
DFT	Relaxed	0	2.1054	3.42514	1.63088/1.62774/1.60432	9.8924
DFT	Pos. I	0	2.09892	3.3155	1.65568/1.65298/1.63824	9.90064
DFT	Pos. II	0	2.10034	3.38928	1.63502/1.63026/1.61682	9.8882

X: Structural model refined against X-ray data
XN: Structural model refined against combined X-ray and neutron data
HR: High resolution diffractometer
IP: Image plate detector
Pos. I: DFT calculations with atomic position of case I
Pos. II: DFT calculations with atomic position of case II

TABLE II: Summary of the MEM calculations at 10 K and corresponding atomic integrated charges.

Case	Description	n χ^n	G	F-pc	Prior	T (K)	Li (e)	B (e)	D1/D2/D3 (e)	BD_4 (e)
1.1	X-HR	2			I	10	2.160	4.009	1.512/1.460/1.429	9.839
1.2	X-HR	2	Y		I	10	2.135	3.910	1.497/1.563/1.446	9.862
1.3	X-HR	2	Y	Y	I	10	2.181	3.244	1.658/1.720/1.588	9.798
1.4	XN-HR	2			II	10	2.239	4.213	1.430/1.392/1.363	9.760
1.5	XN-HR	2			Uniform	10	2.379	3.298	1.391/1.482/1.451	9.073
1.6	XN-HR	2	Y		II	10	2.232	4.256	1.420/1.383/1.354	9.768
1.7	XN-HR	4	Y		II	10	2.225	4.277	1.430/1.375/1.346	9.774
1.8	XN-HR	6	Y		II	10	2.227	4.296	1.427/1.371/1.339	9.771
1.9	XN-HR	2	Y		Uniform	10	-	-	-/-/-	-
1.10	XN-HR	2	Y	Y	II	10	2.231	4.150	1.463/1.401/1.376	9.766
1.11	XN-HR	2	Y	Y	Uniform	10				

n: Order of the statistical central moment of normal residuals of the structure factors
G: Y, if G-constraint is used (125 reflections included in 36 G-groups, 58 independent reflections)
F-pc: Y, if prior-derived F constraints are used

TABLE III: Summary of the MEM calculations at 90 K and corresponding atomic integrated charges.

Case	Description	n χ^n	G	F-pc	Prior	T (K)	Li (e)	B (e)	D1/D2/d3 (e)	BD_4 (e)
2.1	X-HR	2			III	90	2.176	4.092	1.490/1.450/1.396	9.825
2.2	X-HR	2	Y		III	90	2.154	4.091	1.516/1.465/1.386	9.845
2.3	X-HR	2	Y	Y	III	90	2.250	2.992	1.750/1.759/1.619	9.737
2.4	XN-HR	2			IV	90	2.240	4.329	1.397/1.344/1.344	9.757
2.5	XN-HR	2	Y		IV	90	2.237	4.395	1.364/1.325/1.338	9.760
2.6	XN-HR	4	Y		IV	90	2.224	4.421	1.374/1.304/1.338	9.774
2.7	XN-HR	6	Y		IV	90	2.223	4.442	1.375/1.292/1.333	9.774
2.8	XN-HR	2	Y	Y	IV	90	2.239	4.275	1.414/1.330/1.370	9.758
2.9	X-IP	2			V	90	2.198	4.158	1.461/1.360/1.410	9.799
2.10	X-IP	2	Y		V	90	2.170	4.308	1.466/1.359/1.347	9.826
2.11	X-IP	2	Y	Y	V	90	2.250	2.992	1.750/1.759/1.619	9.737
2.12	XN-IP	2			VI	90	2.235	4.295	1.438/1.297/1.368	9.767
2.13	XN-IP	2			Uniform	90	2.280	3.887	1.348/1.305/1.290	9.122
2.14	XN-IP	2	Y		VI	90	2.201	4.522	1.415/1.297/1.282	9.798
2.15	XN-IP	4	Y		VI	90	2.202	4.513	1.406/1.301/1.288	9.796
2.16	XN-IP	6	Y		VI	90	2.207	4.519	1.399/1.296/1.288	9.790
2.17	XN-IP	2	Y		Flat	90	2.208	4.029	1.281/1.077/0.965	8.317
2.18	XN-IP	2	Y	Y	VI	90	2.201	4.496	1.441/1.289/1.287	9.799
2.19	XN-IP	2	Y	Y	Uniform	90	2.208	4.029	1.281/1.077/0.965	8.317

HR data with G-constraint: 113 reflections included in 31 G-groups, 71 independent reflections
IP data with G-constraint: 140 reflections included in 36 G-groups, 41 independent reflections

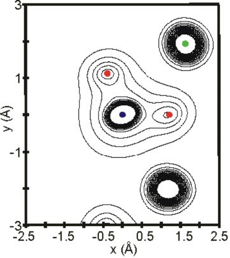
3
1
-1
-3
y (Å)
-2.5
-1.5
-0.5
0.5
1.5
2.5
x (Å)

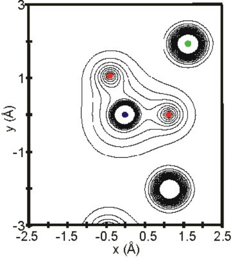
3
1
-1
-3
y (Å)
-2.5
-1.5
-0.5
0.5
1.5
2.5
x (Å)

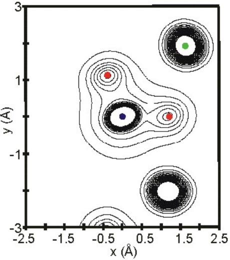
3
1
-1
-3
y (Å)
-2.5
-1.5
-0.5
0.5
1.5
2.5
x (Å)

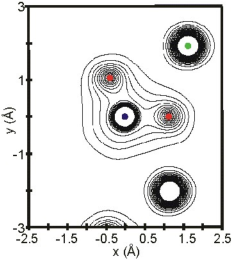
3
1
-1
-3
y (Å)
-2.5
-1.5
-0.5
0.5
1.5
2.5
x (Å)

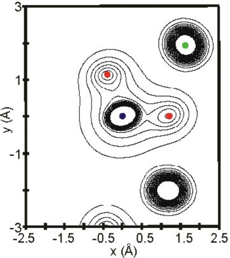
3
1
-1
-3
y (Å)
-2.5
-1.5
-0.5
0.5
1.5
2.5
x (Å)

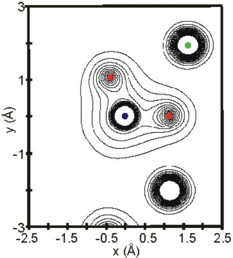
3
1
-1
-3
y (Å)
-2.5
-1.5
-0.5
0.5
1.5
2.5
x (Å)

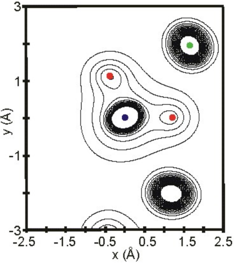
3
1
-1
-3
y (Å)
-2.5 -1.5 -0.5 0.5 1.5 2.5
x (Å)

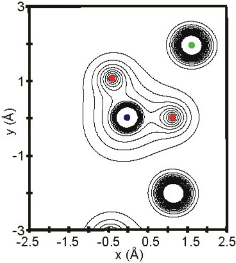
3
1
-1
-3
y (Å)
-2.5 -1.5 -0.5 0.5 1.5 2.5
x (Å)

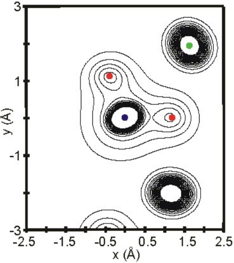
3
1
-1
-3
y (Å)
-2.5 -1.5 -0.5 0.5 1.5 2.5
x (Å)

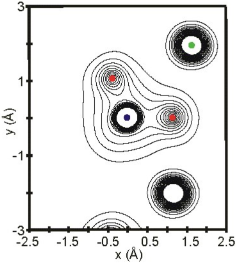
3
1
-1
-3
y (Å)
-2.5 -1.5 -0.5 0.5 1.5 2.5
x (Å)

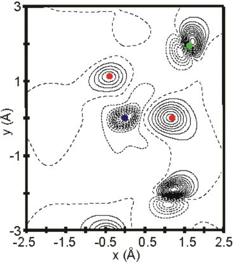
3
1
-1
-3
y (Å)
-2.5 -1.5 -0.5 0.5 1.5 2.5
x (Å)

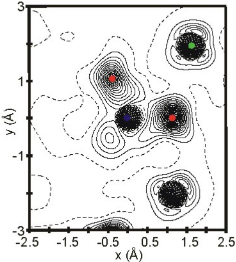
3
1
-1
-3
y (Å)
-2.5 -1.5 -0.5 0.5 1.5 2.5
x (Å)

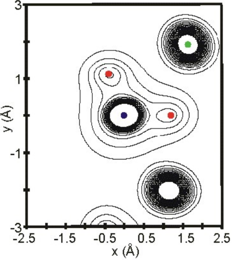
3
1
y (Å)
-1
-3
-2.5
-1.5
-0.5
0.5
1.5
2.5
x (Å)

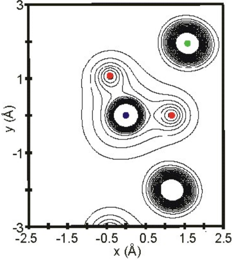
3
1
y (Å)
-1
-3
-2.5
-1.5
-0.5
0.5
1.5
2.5
x (Å)

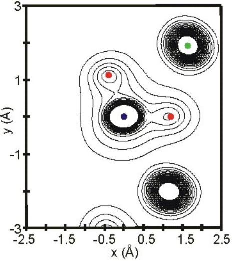
3
1
y (Å)
-1
-3
-2.5
-1.5
-0.5
0.5
1.5
2.5
x (Å)

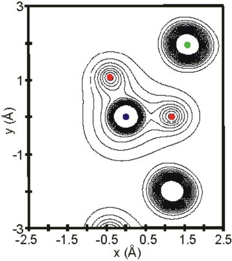
3
1
y (Å)
-1
-3
-2.5
-1.5
-0.5
0.5
1.5
2.5
x (Å)

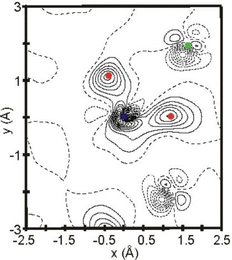
3
1
y (Å)
-1
-3
-2.5
-1.5
-0.5
0.5
1.5
2.5
x (Å)

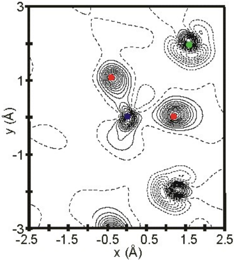
3
1
y (Å)
-1
-3
-2.5
-1.5
-0.5
0.5
1.5
2.5
x (Å)

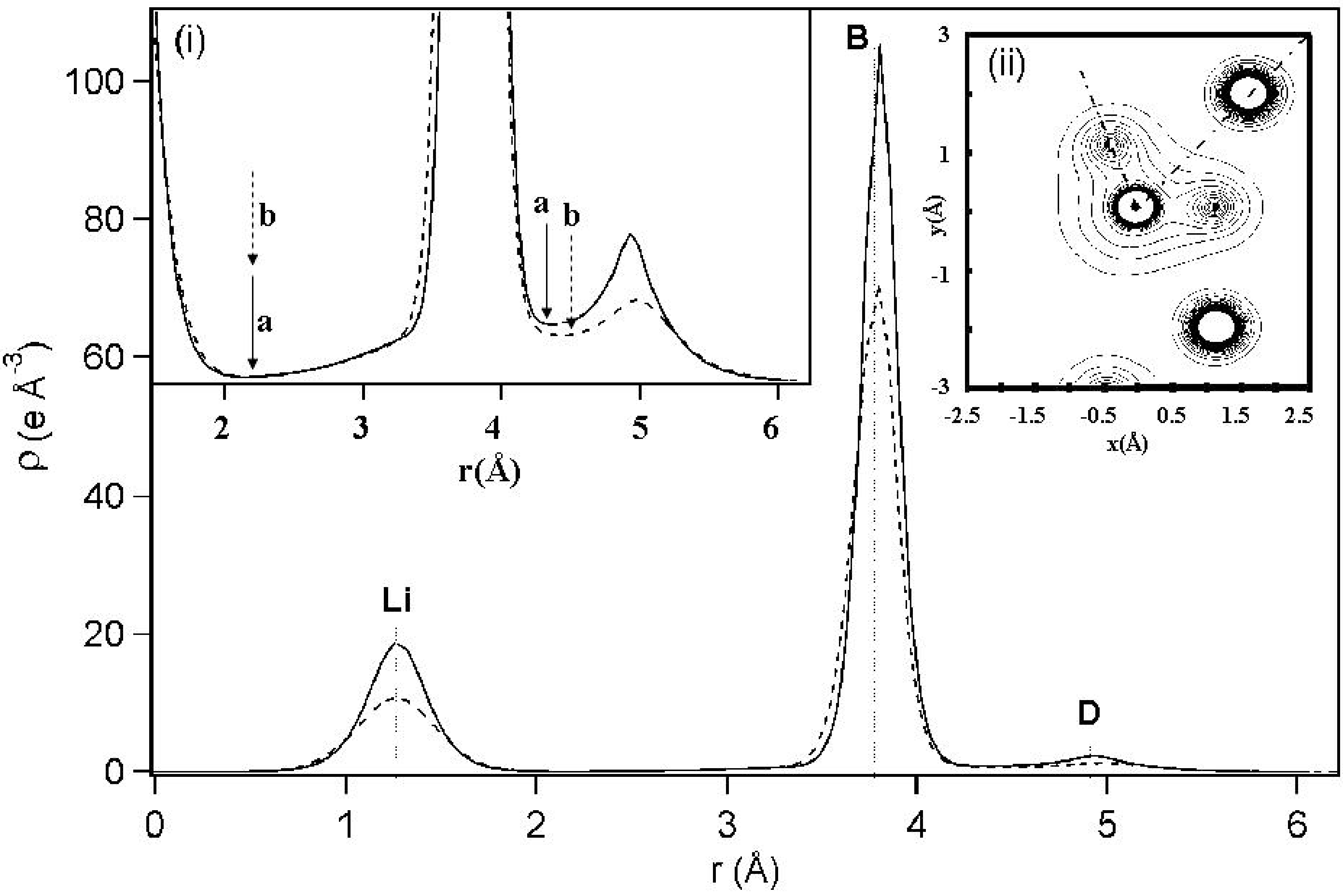
ρ (e Å^{-3})
100
80
60
40
20
0
0
1
2
3
4
5
6
r (Å)
Li
B
D
(i)
b
a
a
b
2
3
4
5
6
r(Å)
(ii)
3
1
-1
-3
y(Å)
-2.5
-1.5
-0.5
0.5
1.5
2.5
x(Å)

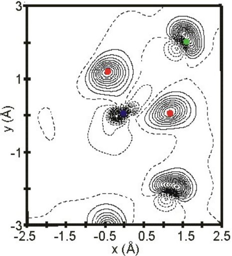
3
1
-1
-3
y (Å)
-2.5
-1.5
-0.5
0.5
1.5
2.5
x (Å)

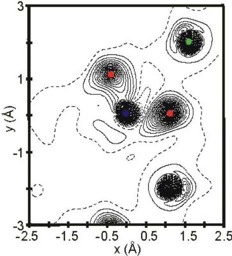
3
1
-1
-3
y (Å)
-2.5
-1.5
-0.5
0.5
1.5
2.5
x (Å)

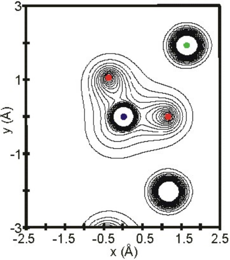
3
1
-1
-3
y (Å)
-2.5 -1.5 -0.5 0.5 1.5 2.5
x (Å)

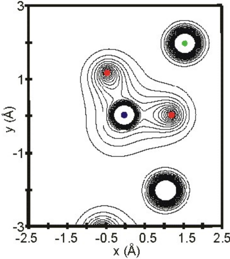
3
1
-1
-3
y (Å)
-2.5 -1.5 -0.5 0.5 1.5 2.5
x (Å)

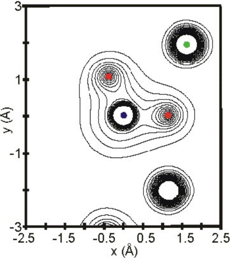
3
1
-1
-3
y (Å)
-2.5 -1.5 -0.5 0.5 1.5 2.5
x (Å)

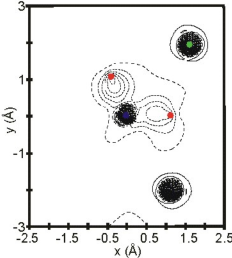
3
1
-1
-3
y (Å)
-2.5 -1.5 -0.5 0.5 1.5 2.5
x (Å)